Materials Advances

ROYAL SOCIETY OF CHEMISTRY

PAPER

View Article Online
View Journal | View Issue

Check for updates

Cite this: *Mater. Adv.*, 2025, 6, 448

Nickel-free porous stainless-steel nanocomposites for versatile biomedical applications: fabrication, characterization, and evaluation of electrochemical and immunogenicity detection

Sabreen Abdallah Abdelwahab,[a] Mohamad Warda,[bc] Mamdouh Zewaid,[a] Hisham Saleh,[d] Omar A. Ahmed-Farid,[e] Hassan A. M. Hendawy,[f] Elbadawy A. Kamoun, *[gh] Amr Negm, [gi] Jong Yeog Son *[j] and Ahmed I. Ali *[jk]

This study focuses on the development of nickel-free stainless-steel nanocomposites with porosities tailored for surgical implants and biological applications. Alloy F2581 (Fe–17Cr–10Mn–3Mo–0.4Si–0.5N–0.2C wt%), modified by replacing Mo with metals such as Al, Cu, Ti, and W, was successfully fabricated *via* a solid-state reaction method. X-ray diffraction analysis revealed a significant alteration in the crystal phase, accompanied by the formation of nanostructures, including nanowires, square nanotubes, wave-like configurations reminiscent of a growing clover farm, and nanofibers. The particle sizes of these structures were determined to be 73, 27.2, 76 and 98.5 nm for Al, Cu, Ti, and W ions, respectively, indicating a distribution of nanopores. Biological evaluation of adult male *Albino* rats after exposure to single intraperitoneal doses of various concentrations (10, 20, and 50 mg kg^{-1} wt%) were assessed with testing alloys (Cu, Al, W, and Ti, respectively). Over a subacute period lasting 60 days, a comprehensive evaluation of biological responses, including hepatic function, renal performance, oxidative and/or nitrosative stress parameters, and the levels of serum immune modulators was conducted. Notably, low doses elicited negligible immune responses, higher doses, barring copper, induced notable reactions. Interestingly, aluminum demonstrated optimization within biological settings, alongside titanium and tungsten. These findings highlight the applicability of copper and tungsten for medical implantation and biological applications under controlled circumstances, particularly at lower dosage levels.

Received 11th October 2024,
Accepted 29th November 2024

DOI: 10.1039/d4ma01024h

rsc.li/materials-advances

Open Access Article. Published on 12 December 2024. Downloaded on 4/2/2026 4:53:51 PM.
This article is licensed under a Creative Commons Attribution 3.0 Unported Licence.

[a] *Production Technology Department, Faculty of Technology and Education, Helwan University, Saray El-Quba, 11281 Cairo, Egypt*
[b] *Department of Biochemistry and Molecular Biology, Faculty of Veterinary Medicine, Cairo University, Giza, 12211, Egypt*
[c] *Department of Physiology, Faculty of Veterinary Medicine, Ataturk University, Erzurum, Turkey*
[d] *Solid State Physics, Physics Deviation, National Research Center, El Bahous St., Giza, Cairo, Egypt*
[e] *Physiology Department, National Organization for Drug Control and Research (NODCAR), Giza, Egypt*
[f] *Analytical and Inorganic Chemistry Department, NODCAR, Giza, Egypt*
[g] *Department of Chemistry, College of Science, King Faisal University, Al-Ahsa 31982, Saudi Arabia. E-mail: ekamoun@kfu.edu.sa, badawykamoun@yahoo.com*
[h] *Polymeric Materials Research Dep., Advanced Technology and New Materials Research Institute (ATNMRI), City of Scientific Research and Technological Applications (SRTA-City), New Borg Al-Arab City 21934, Alexandria, Egypt*
[i] *Chemistry Department, Faculty of Science, Mansoura University, Mansoura 35516, Egypt*
[j] *Department of Applied Physics and Institute of Natural Sciences, College of Applied Science, Kyung Hee University, Suwon 446-701, Republic of Korea*
[k] *Department of Basic Science, Faculty of Technology and Education, Helwan University, Saray El-Quba, 11281 Cairo, Egypt. E-mail: Ahmed_Ali_2010@techedu.helwan.edu.eg*

1. Introduction

The growing demand for biomedical implants, driven by the increasing number of orthopedic procedures annually, necessitates the development of diverse bone scaffolds and augmentations.[1–3] These implants should be similar to the mechanical and microstructural properties of natural bone to substantially improve the remediation process.[1–6] Generally, humanoid bones are categorized into two types (*i.e.*, trabecular and cortical bones). The trabecular bones, situated within bone centers, feature a plethora of interconnected and equiaxed pores spanning hundreds of micrometers in diameter. Compared with those of cortical bone, their high porosity results in lower mechanical properties.[7–10]

The porous structure and composition of scaffolds dictate cellular responses such as adhesion, penetration, differentiation, nutrient diffusion, and bone ingrowth.[11–18] Furthermore, biomaterials essentially need corrosion resistance, wear resistance, and biocompatibility and to possess strong osseointegration, which is the ability to combine with bone and

© 2025 The Author(s). Published by the Royal Society of Chemistry

Open Access Article. Published on 12 December 2024. Downloaded on 4/2/2026 4:53:51 PM.
This article is licensed under a Creative Commons Attribution 3.0 Unported Licence.

other tissues, which is a good biological environment for the effective movement of medications, and good hardness, tensile strength, and elongation, while being extremely nontoxic and/or anti-allergenic.[12–14] Metal alloys are widely used as biomaterials. Iron alloys containing at least 11% anti-rusting chromium, which also increases heat resistance,[19] with less than 1.2% carbon, and other alloying components are known as stainless steels. The mechanical qualities can be enhanced by additive elements like nickel, molybdenum, niobium, manganese, titanium, copper, aluminum, and tungsten. Moreover, the corrosion resistance and mechanical qualities of stainless steel can be further improved.[20] The inclusion of Cr and Mo is responsible for the exceptional biocompatibility, mechanical qualities (strength and ductility), and resistance to pitting and crevice corrosion of the material.[21]

Porous stainless steel represents one of the most important metal alloys used in the manufacture of biomaterials. It can contribute to lightweight materials with excellent mechanical, thermal, and electrical properties.[22] Ferrous metals have found widespread application in the fabrication of stents and dental and orthopedic implants, including bone plates, fixtures, dental posts, and screws, as well as surgical instruments. However, the release of iron (Fe) ions can lead to interactions with peroxides, leading to the generation of radicals. This phenomenon can have deleterious consequences, potentially culminating in severe outcomes such as coma or fatality owing to the deleterious produces of free radicals on lipids, proteins, DNA, and ultimately, cellular integrity.[23] Owing to its comparatively lower cost than those of cobalt–chromium alloys, pure titanium, and titanium alloys, 316 L stainless steel is frequently employed in orthopedic implants. Its utilization in this context is observed at a ratio ranging from ten-to-five.[24] While numerous studies have explored the mechanical and microstructural properties of trabecular bone, replicating these properties in materials poses a significant challenge. Metals like stainless steel, Co–Cr alloys, and titanium alloys are commonly utilized in the production of various biomedical implants.[25] However, achieving the desired porosity in these materials is difficult because of their high melting points, which limits the usage of conventional manufacturing techniques such as casting. Several studies have investigated the fabrication of porous stainless steel *via* conventional methods like casting and powder metallurgy, but these approaches present significant challenges. To overcome these challenges, researchers have explored alternative techniques, including rapid prototyping[26] and the sol–gel method.[27] For example, Mariotto *et al.* synthesized steel foam samples containing 30% ammonium carbonate and conducted electrochemical tests in a chloride-containing medium, comparing the corrosion resistance of the foam samples to that of bulk steel. The results indicated that the corrosion resistance of foam samples was superior to that of the bulk steel.[28] Noor *et al.* reported that porous SS316L has no cytotoxic potential for biomedical implants.[29] Babaie *et al.* produced a sample with a tight pore structure and a multimodal pore size, but the samples were subjected to a cytotoxicity test.[18] Other studies have used powder metallurgy to produce porous stainless steel. Dewidar *et al.* produced highly porous 316 L stainless steel samples whose mechanical properties match those of human bone.[30] Salahinejad *et al.* manufactured porous Cr–Mn–N austenitic stainless steel, and nanostructured austenitic stainless steel was developed with a comparative density of 85%.[31] Dudek *et al.* discussed the chances of obtaining materials with controllable porosity. The samples produced in hydrogen and under vacuum have high corrosion resistance and high porosity, and these samples can be used for medical purposes.[32] Essa *et al.* investigated porosity content control in capsule-free powder and reported a substantial increase in the pore fraction of the samples with increasing powder particle size, which was related with a decrease in the compressive strength, elastic modulus, hardness, and ductility of the samples.[21] Zielecka *et al.* developed a porous stainless steel that exhibited extreme porosity in comparison to other ingredients, and the allocation of pores was classified as micropores.[33] The samples produced can be used in biomedical applications because their properties simulate those of human bones.[34] Weipeng *et al.* fabricated Fe–Cr–N stainless steel *via* powder metallurgy, achieving porosities ranging from 28.21% to 60.16%. This stainless steel exhibited high biocompatibility, corrosion resistance, and mechanical properties comparable to those of human bone, which was attributed to its nonnickel and manganese composition. The pore morphology, microstructure, and mechanical characteristics of the porous stainless steel were thoroughly analyzed. As the porosity increased, the compressive yield strength, elastic modulus, and compressive strength decreased.[35] Moreover, rapid prototyping methodologies offer promising avenues for fabricating materials with structural similarities to trabecular bone.[36,37] In the realm of biomaterials, considerable attention has been given to Ti- and- Co-based alloys, because of their notable biocompatibility and robust mechanical properties.[38,39] Tungsten implants, categorized within the refractory metal class, demonstrate exceptional resistance to both heat and corrosion, rendering them suitable for bone fracture applications.[40] Investigations into the clinical efficacy of alumina substrates have also been undertaken.[41]

Copper is renowned for its potent antimicrobial properties and is frequently employed as a filter. To enhance antibacterial efficacy and ensure optimal biocompatibility in orthopedic implants, precise dosages of copper must be incorporated into titanium and other metallic materials. Currently, copper ions and metallic copper represent the two primary forms utilized in biomaterials, both of which exhibit robust antibacterial capabilities. Additionally, copper ions are known to impede DNA replication and protein synthesis.[42]

This study aims to investigate the physiochemical characteristics of porous stainless steel samples synthesized through a solid-state reaction method, wherein molybdenum is replaced with various elements, including copper, aluminum, titanium, and tungsten, in accordance with ASTM F2581 standards (Fe–17Cr–10Mn–3MX–0.4Si–0.5N–0.2C in wt%; MX: Al, Cu, Ti, and W) for medical implantation and biological applications. Characterization of samples was performed *via* XRD, FT-IR, and SEM analyses. Furthermore, the electrochemical kinetic parameters are determined *via* dynamic polarization techniques

Open Access Article. Published on 12 December 2024. Downloaded on 4/2/2026 4:53:51 PM. This article is licensed under a Creative Commons Attribution 3.0 Unported Licence.

and electrochemical frequency modulation (EFM). The subacute effects of administering single intraperitoneal doses of the examined alloys at concentrations of 10, 20, and 50 mg kg^{-1} to a rat animal model were subsequently investigated over a period of 60 days. The assessment involves monitoring the serum activities of the liver enzymes alanine transaminase (ALT) and aspartate transaminase (AST) to evaluate liver function. Additionally, the serum creatinine levels reflect renal performance in the experimental rats. Furthermore, hepatic superoxide dismutase (SOD) activity and reduced glutathione levels are assessed to evaluate global oxidative stress, whereas nitric oxide (NO) levels serve as indicators of nitrosative stress. The levels of serum cortisol, a primary stress hormone, are measured along with the levels of the immunomodulators interleukin 1 (IL1) and interleukin 10 (IL10) to elucidate the cellular immune response to each injected alloy.

2. Materials and methods

2.1. Materials

Powders of FeCl, MnO_2, CrCl, SiO_2, NiO, C, and metal oxides (MX) *e.g.* (MX: CuO, WO_2, TiO_2 and Al_2O_3) were purchased from Sigma-Aldrich Limited and Al-Gomhouria Chemical Company in Cairo, Egypt. All powders were mixed in an agate mortar with stoichiometric ratios (with composition of ASTM F2581: (Fe–17Cr–10Mn–3MX–0.4Si–0.5 N–0.2C in wt%)) and sintering aid (Mn–11.5 wt% Si) powders.

2.2. Preparation of porous stainless-steel composites

Four sets of samples were prepared by substituting MX with four additive composite materials in powder form. The mixtures were ground in an agate mortar for 40 minutes until well blended, followed by dissolution in methanol through ultra-sonication, and the powders were manually ground by hand to achieve a homogeneous mixture before proceeding with dissolution. The solutions were subsequently heated *via* a magnetic stirrer at 80 °C for approximately 2–3 h to evaporate the alcohol and dry the samples. Manual grinding in an agate mortar was then performed for two hours to achieve a fine powder consistency. The samples were calcined in an alumina crucible at 600 °C for 3 h with a heating rate of 7 °C in a closed programmable muffle box furnace (Fengshi made in Germany, with a chamber size of 400 × 400 × 500 mm $W \times H \times D$), followed by gradual cooling to room temperature naturally. Afterward, further grinding was carried out for an hour and sieved using a 100-μm mesh screen. Furthermore, the samples were compressed *via* a hydraulic press at a pressure of 5 tons cm^{-2} for 5 min in a forming die, resulting in samples with dimensions of 10 mm, and 1–1.5 mm in diameter and thickness, respectively. Finally, the samples were sintered in a muffle furnace at 1150 °C for 6 h, followed by quenching in air (Scheme 1).

2.3. Electrochemical corrosion

The samples were prepared in the form of an electrode (2.0 × 5.0 mm diameter) *via* a hand press. A group of samples was prepared for the purpose of measuring electrochemical corrosion products to obtain samples for conducting an electrochemical corrosion test on a stainless-steel pallet, which was conducted after 5 min as it was ready to perform the required examination.

2.4. Instrumental characterization

2.4.1. Physical characterization. Structural properties of synthesized nanoparticles were analyzed *via* an X-ray diffractometer (Rigaku Ultima IV) equipped with a CuKα radiation

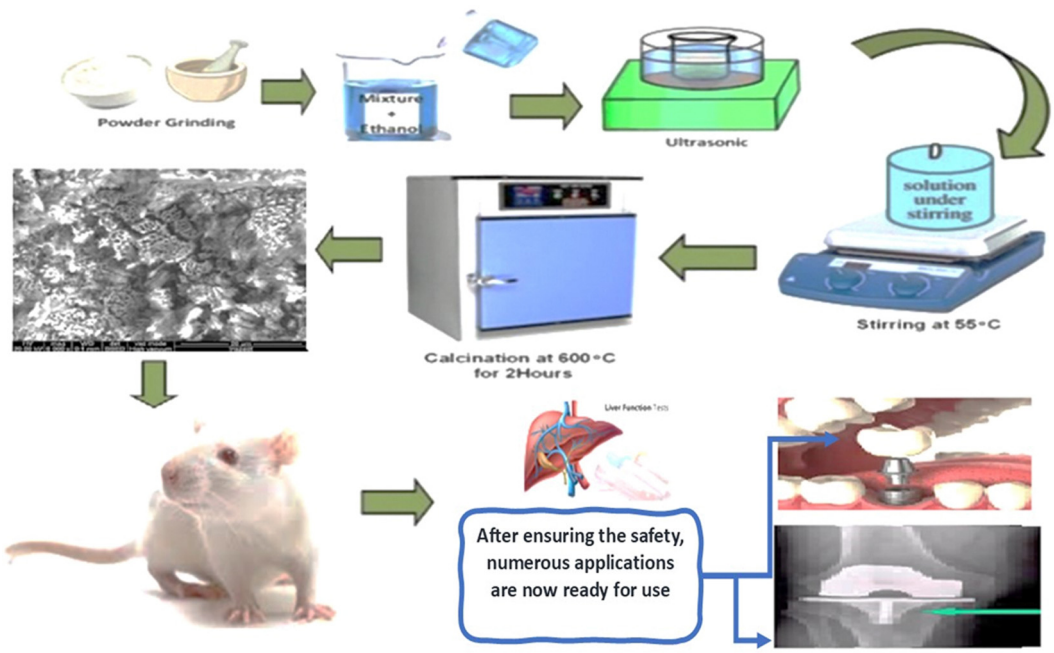

Scheme 1 Schematic diagram representing preparation steps and applications of nickel-free porous stainless-steel nanocomposites.

© 2025 The Author(s). Published by the Royal Society of Chemistry

Open Access Article. Published on 12 December 2024. Downloaded on 4/2/2026 4:53:51 PM. This article is licensed under a Creative Commons Attribution 3.0 Unported Licence.

source (λ = 1.541 Å) operating at 40 kV and 40 mA. Scans were conducted over a 2θ range from 10° to 80° at a scanning rate of 5° min^{-1}. The relative abundance of phases present and the crystallite size were determined through Rietveld analysis. A precisely known quantity of nanocrystalline powder served as the standard reference, as previously described.[43] The surface morphology (shape and size of the nanoparticles) of the synthesized samples was determined *via* FE-SEM (Model-Quanta FEI200, FE-SEM). Fourier transform infrared (FT-IR) spectroscopy was performed with a Mattson 5000 spectrometer (Unicam, UK) *via* the KBr technique (transmission mode with 0.5 mg sample and 100 mg KBr ratio, due to the sample being highly absorbed).

2.4.2 Electrochemical corrosion characterization. Bones undergo perpetual immersion in bodily fluids such as blood, which are characterized by diverse acidic and saline constituents. This prolonged exposure results in erosion and subsequent release of its structural components. Evaluating the composition and quantities of the elements liberated in various liquid environments, which mimic those encountered by natural bones, is imperative. Electrochemical corrosion resistance serves as a pivotal parameter for gauging the endurance or robustness of a bone–alloy metal composite within the physiological milieu, given the array of chemical reactions involving cathodic and anodic processes. Notably, the reduction of dissolved oxygen emerges as a consequential cathodic reaction, represented by the following equation:

$$O_2 + 2H_2O + 4e^- \rightarrow 4OH^- \quad (1)$$

The reduction of hydrogen ions is another associated reaction, depicted by the following equation:

$$2H^+ + 2e^- \rightarrow H_2 \quad (2)$$

One of the critical anodic reactions involves the oxidation of metals employed in bone materials, resulting in the formation of molten or solid erosion byproducts. An essential criterion for any alloy intended for bodily use is its ability to avoid generating corrosion products that might pose risks to the organism. While certain metallic elements are deemed safe under ordinary circumstances, they have the potential to produce toxic ions or compounds. Therefore, samples were measured and examined *via* the Gamry REF 3000 potentiostat/galvanostat/Zra instrument for data acquisition, alongside Echem Analyst 7.8.2 for comprehensive analysis, synthesis, and graphical representation. Electrochemical kinetic parameters were acquired through two distinct methodologies: potentio-dynamic polarization techniques and electrochemical frequency modulation (EFM). Electrochemical corrosion products were analyzed at the National Organization for Drug Control and Research (NODCAR). Following a storage period of one week, models were established to perform electrochemical corrosion testing *via* voltammetry (Metrohm 797 VA Computrace for trace analysis). The reference electrode utilized was Ag/AgCl, with a platinum auxiliary electrode. The test medium consisted of an electrolyte solution comprising serum at a pH of 7.40 (representative of 50% biological body fluids) supplemented with phosphate-buffered saline,[44,45] and the temperature used is 37.0 ± 0.1 °C.

The chloride ion concentrations in the serum and urine were within the range of 105–125 mmol L^{-1}. Electrolyte solutions containing 10% serum with a pH of 7.40 and phosphate-buffered saline were prepared for electrochemical measurements, with temperature control ensured *via* a water bath. All test electrolytes were prepared without any nonaerated treatments, and samples were analyzed in triplicate to ensure accuracy and reproducibility. Ethical considerations were strictly adhered to throughout the collection and handling of biological samples. Voltammetry measurements of the polarization curves were conducted within the E_{corr} ± 250 mV range at a scan rate of 10 mV s^{-1}. Steady-state cyclic polarization curves were obtained over the potential range of −800 to +200 mV *versus* E_{corr}, with a scan rate of 0.5 mV s^{-1}. Periodic polarization curves were also obtained within the potential range of −800 to +200 mV *versus* E_{corr} at a scan rate of 10 mV s^{-1}.

2.5. Biological tests

Human urine and serum were ethically collected from healthy subjects who provided the signed consents of the donors, according to the ethical rules of research in Egyptian universities. The participants underwent routine health check-ups, and no known chronic diseases were present in the cohort. The total number was five male participants, aged between 35–45 years. Inclusion criteria comprised male participants aged 35–45 years with no history of chronic diseases, who were generally healthy and underwent routine health check-ups. Exclusion criteria included individuals with a history of chronic conditions such as diabetes, hypertension, cardiovascular diseases, kidney or liver diseases, any acute illness at the time of the study, or those on medications that could affect the study outcomes. The serum and urine samples collected averaged 5 mL of serum and 20 mL of urine per participant, respectively.

Animal study: adult male *Albino* rats, weighing approximately 150 ± 15 g, were employed for this study. The rats were housed in the animal facility of the National Organization for Drug Control and Research for seven days prior to the experiment, where they were maintained under standard laboratory conditions with *ad libitum* access to food and water. The experimental procedures were conducted in accordance with the ethical guidelines set forth by the Institutional Animal Care and Use Committee at the Faculty of Veterinary Medicine, Cairo University (Vet. Cu. IACUC), with approval number Vet. CU. 09092023786.

2.5.1. Experimental design. Following the acclimatization period, the rats were divided into five groups, each comprising six animals. Group 1 served as the control and received a basal diet, whereas groups 2–10 were subjected to single intraperitoneal dosing with varying concentrations (10, 20, and 50 mg kg^{-1} BW) of the investigated alloys (Cu, Al, W, and Ti).

2.5.1.1. Blood sample collection. Blood samples were collected from each rat's retro-orbital vein under light diethyl ether anesthesia, as described by Cocchetto *et al.*[46] After clotting, the blood was

Open Access Article. Published on 12 December 2024. Downloaded on 4/2/2026 4:53:51 PM. This article is licensed under a Creative Commons Attribution 3.0 Unported Licence.

centrifuged at 3000 rpm for 15 min to obtain the serum. The serum was then utilized for assessing liver enzyme activities, monitoring kidney function, and evaluating stress and immune response parameters.

2.5.2. Preparation of liver samples. Following blood sampling, the animals were euthanized by cervical dislocation, and their liver tissues were promptly exercised, rinsed with ice-cooled saline, blotted dry, and weighed. A portion of each liver sample was then homogenized with ice-cold saline (0.9% NaCl) *via* a homogenizer (Medical Instruments, MPW-120, Poland) to obtain a 20% w/v homogenate. The homogenate was subsequently centrifuged for 5 minutes at 4000 rpm, and the resulting aliquot was utilized for the assessment of SOD, GSH, and NO.

2.5.2.1. Measurement of liver enzyme activities in serum. Liver function was assessed by quantifying the serum levels of ALT and AST enzymes, which are reliable markers of liver function, *via* Egyptian Company for Biotechnology (S.A.E), Obour City Industrial Area, Block 20008, Piece 19 A, Cairo, Egypt kits. The results are reported in units per liter (U L^{-1}).[47]

2.5.3. Assessment of antioxidant status by measuring SOD activity. Spectrophotometric analysis was employed to measure superoxide dismutase (SOD) activity,[48] allowing for the evaluation of the antioxidant defense against superoxide radicals. SOD activity serves as an indirect marker of oxidative stress, a condition that can potentially lead to lipid peroxidation. This spectrophotometric quantification method is based on the inhibition of pyrogallol autoxidation at 325 nm, where pyrogallol undergoes autoxidation in the presence of oxygen, producing superoxide radicals that are dis-mutated by SOD into oxygen and hydrogen peroxide. The assay was conducted within a linear range of 0.05–2.5 U mL^{-1} SOD activity, with one unit (U) defined as the amount of enzyme causing 50% inhibition of pyrogallol autoxidation under optimal conditions (pH 8.0–8.2). The method demonstrated high specificity for SOD activity, a detection limit of 0.01–0.05 U mL^{-1}, and excellent reproducibility with coefficients of variation (CV) below 2%.

The concentration of reduced glutathione (GSH) and oxidized glutathione (GSSG) was determined using high-performance liquid chromatography (HPLC) based on the method outlined by Jayatilleke and Shaw (1993).[49] Reference standards for GSH and GSSG were obtained from Sigma Chemical Co. and prepared as stock solutions (1 mg mL^{-1}) in 75% methanol. These stock solutions were diluted as necessary before injection into the HPLC system. The analysis was performed using an Agilent HPLC system, equipped with a quaternary pump, column oven, Rheodyne injector with a 20 μL loop, and a UV variable wavelength detector. Data analysis and chromatograms were generated using ChemStation software (Agilent). Separation was achieved on a Synergi RP Max column (3.9 mm), with detection at 210 nm. The mobile phase was an isocratic mixture of potassium phosphate buffer and acetonitrile at pH 2.7, with a flow rate of 2 mL min^{-1}, whereas the nitric oxide (NO) concentration (in nmol g^{-1} tissue) was determined *via* HPLC according to Papadoyannis *et al.* (1999).[50] NO was determined as the summation of nitrite and nitrate; the HPLC method involved preparing reference standard solutions with a stock concentration of 1 mg mL^{-1} for each sodium nitrite and sodium nitrate. A standard mixture containing equal concentrations of nitrite and nitrate was prepared to determine retention times and achieve peak separation. Samples were analyzed using an Agilent HP 1100 series HPLC system (USA) with a PRP-X100 Hamilton anion exchange column (150 × 4.1 mm, 10 μm). The mobile phase consisted of a mixture of 0.1 M NaCl and methanol in a 45 : 55 volume ratio, with a flow rate of 2 mL min^{-1}, and detection was performed at 230 nm.

2.5.4. Determination of stress factor and immune response element parameters in the serum. Cortisol, (Cloud-Clone Corp. (China) model: SEA056Hu) a stress factor, and the levels of the immune response elements IL-1 (Cusabio Technology LLC (China), model: CSB-E13066h) and IL-10 (Elabscience Biotechnology Co., Ltd (China) model: E-EL-H0149) were quantified *via* laboratory available enzyme-linked immunosorbent assay (ELISA) kits following the manufacturers' instructions.

3. Results and discussion

3.1. X-ray diffraction

Fig. 1(a) shows the XRD pattern of sintered samples of F2581: (Fe–17Cr–10Mn–3MX–0.4Si–0.5 N–0.2C wt%) with MX additives, including (a) Cu, (b) W, (c) Ti, and (d) Al. Rietveld analysis of the XRD data reveals the formation of a single-phase austenitic structure following sintering at 1100 °C. Notably, samples were quenched in water to attain the austenitic structure after sintering. The relatively low signal-to-noise ratio in the XRD pattern was attributed to the presence of amorphous phase in the material. Furthermore, XRD analysis (Fig. 1) reveals the presence of Fe and Al phases, as evidenced by the curve patterns, with no intermetallic phase detected. Additionally, the mean crystallite size was determined to be less than 98.5 nm (73, 27.2, 76, and 58 nm for Al, Cu, Ti, and W, respectively), which is consistent with previous studies employing various methods for the preparation of nanostructured powders.[45,51] Microscopic studies further confirmed the presence of this nanoscale structure even after the sintering process, reflecting a significant reduction in grain growth.[52,53]

3.2. FT-IR spectroscopy

FT-IR spectra of the prepared F2581 (Fe–17Cr–10Mn–3MX–0.4Si–0.5 N–0.2C in wt%) samples containing MX = (a) Cu, (b) W, (c) Ti, and (d) Al additives are shown in Fig. 1(b). The samples exhibited single-phase austenitic structures; the samples with metal elements presented peaks related to the crystalline planes as shown in the XRD patterns that were linked to the austenitic iron structure of all the samples. The crystallite size and phase percentages were calculated *via* Rietveld analysis of the XRD results. The structures of the samples were further confirmed by FT-IR spectroscopy, as shown in Fig. 1(b). The FT-IR spectra of all sample nanoparticles were recorded in ν 400–4000 cm^{-1}. The characteristic stretching modes of C═O and C–O bonds are assigned to the significant bands at ν 1130 and 1730 cm^{-1} vibrations, respectively. The peak at ν 2962 cm^{-1}

 © 2025 The Author(s). Published by the Royal Society of Chemistry

Open Access Article. Published on 12 December 2024. Downloaded on 4/2/2026 4:53:51 PM.
This article is licensed under a Creative Commons Attribution 3.0 Unported Licence.

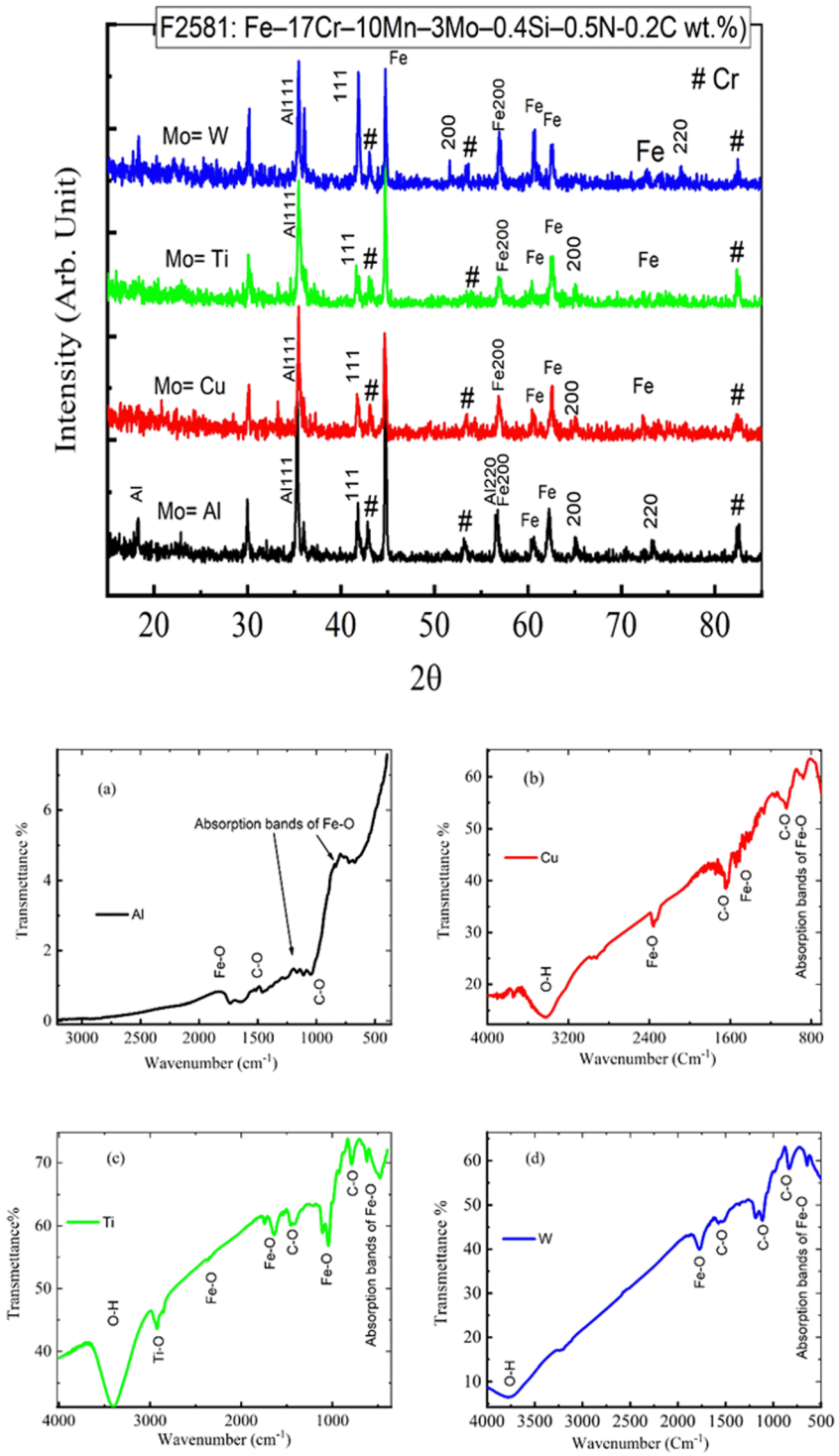

Fig. 1 XRD powder patterns (up) and FT-IR transmittance (down) (a, b, c, and d) of an alloy composed of (Fe–Cr–Si–Ni–Mn–C), with doped elements including Al, Cu, Ti, and W ions; respectively.

can be attributed to the aromatic stretching mode. The transmittance bands at ν 3459 and 3478 cm^{-1} arise from the stretching mode of the O–H group, which reveals the existence of a small amount of water absorbed by the nanostructure. The peak shift observed at approximately ν 1117 cm^{-1} to a higher wavenumber of ν 1130 cm^{-1} corresponds to the Al, Cu, W, and Ti additives in F2581: (Fe–17Cr–10Mn–3MX–0.4Si–0.5 N–0.2C in wt%) samples in the host lattice.[54–58]

3.3. FE-SEM investigation

The morphological features of the synthesized F2581 samples (Fe–17Cr–10Mn–3MX–0.4Si–0.5N–0.2C wt%) with various metal

Open Access Article. Published on 12 December 2024. Downloaded on 4/2/2026 4:53:51 PM. This article is licensed under a Creative Commons Attribution 3.0 Unported Licence.

additives (MX) such as Cu, W, Ti, and Al were characterized using field emission scanning electron microscopy (FE-SEM). The SEM images at a magnification of 6000× provided detailed insights into the nanoscale morphology and uniformity of the samples, offering a better understanding of how these metal additives influence the microstructural characteristics of the nanocomposites.

3.3.1. Al additive (Fig. 2a). The FE-SEM images of the Al-doped sample revealed that the nanoparticles predominantly form nanowires. This unique morphology could be attributed to the specific interaction of aluminum with the matrix during synthesis, promoting the growth of wire-like structures. The presence of these nanowires indicates a high surface area, which may have implications for improving the material's mechanical properties, such as strength and wear resistance. Notably, the 6000× magnification image also showed the presence of small pores, which suggests the formation of a porous network. This porosity could be a beneficial feature for applications where lightweight and high surface area materials are desirable, such as in catalysis or filtration systems.

3.3.2. Cu additive (Fig. 2b). The Cu-doped sample exhibited a distinct square nanotube shape. The SEM images showed that these nanotubes were well-formed, with a regular square or rectangular cross-sectional shape. This morphology is indicative of the influence of copper in promoting specific growth mechanisms during the formation of the composite. The distribution of pores within the nanotubes could potentially enhance the material's mechanical properties, as the interconnected porosity might lead to improved impact resistance. The presence of well-dispersed pores in all Cu-containing composites further suggests that copper could assist in controlling the microstructure and pore size, leading to enhanced performance in structural applications.

3.3.3. Ti additive (Fig. 2c). The FE-SEM images of the Ti-doped sample revealed nanoparticles with a wavy, clover-like morphology. This distinctive shape could be the result of the interaction between titanium and the surrounding matrix, influencing the nucleation and growth phases during synthesis. The uniform distribution of these particles at the nanoscale, along with the well-formed pores, suggests that titanium plays a crucial role in the control of particle shape and size. The wavy morphology could have potential implications for enhancing the material's mechanical properties, such as flexibility or resistance to cracking, making it suitable for use in more dynamic, load-bearing applications.

3.3.4. W additive (Fig. 2d). In the case of the W-doped sample, the FE-SEM images revealed the formation of nanofibers, which is a highly desirable structure in various engineering materials due to its high surface area and strength-to-weight ratio. The uniform distribution of pores within these nanofibers suggests that tungsten plays a significant role in promoting fiber-like growth during the synthesis process. The porosity in this sample could contribute to improving thermal and electrical conductivity, as well as enhanced mechanical properties such as toughness, making these composites particularly useful for high-performance applications such as in electronics or high-temperature environments.

3.3.5. Comparison of additives. When comparing the four additives—Al, Cu, Ti, and W—several trends emerge. Each additive significantly influences the morphology and pore structure of the composites, resulting in distinct shapes, such as nanowires, nanotubes, wavy particles, and nanofibers. The additives contribute to the creation of nanostructures with varying degrees of uniformity, pore distribution, and surface area. These differences in morphology directly affect the physical properties of the composites, such as their mechanical strength, corrosion resistance, and thermal conductivity, which will be further explored in the electrochemical corrosion tests (Section 3.4). The SEM analysis also indicates that the powder

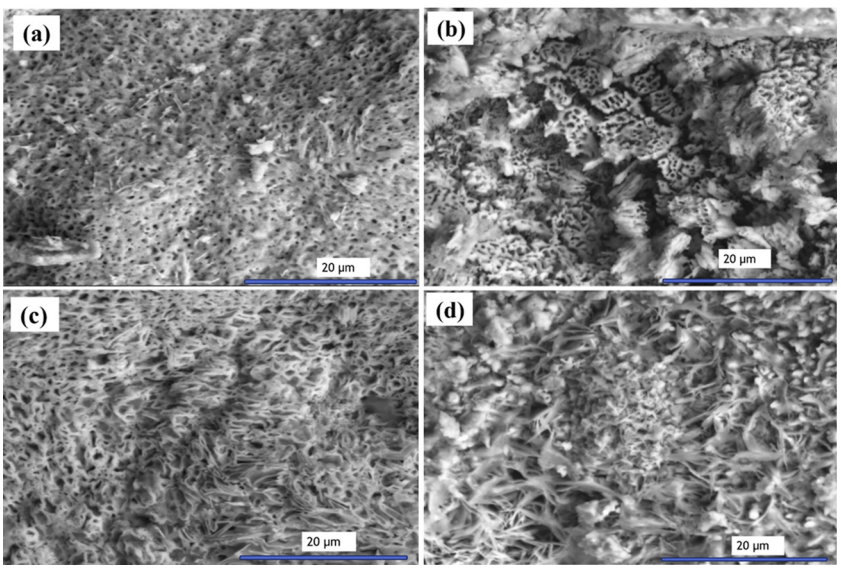

Fig. 2 FE-SEM images of doped samples at the original magnification (6000×) (a) Al (Fe–Cr–Si–Ni–Mn–C), (b) Cu (Fe–Cr–Si–Ni–Mn–C), (c) Ti (Fe–Cr–Si–Ni–Mn–C), and (d) W (Fe–Cr–Si–Ni–Mn–C).

 © 2025 The Author(s). Published by the Royal Society of Chemistry

Open Access Article. Published on 12 December 2024. Downloaded on 4/2/2026 4:53:51 PM. This article is licensed under a Creative Commons Attribution 3.0 Unported Licence.

metallurgy method is effective in producing these complex microstructures, which is promising for large-scale industrial applications due to its low cost and environmental benefits.

3.4. Electrochemical corrosion test

The electrochemical behavior of the synthesized alloys was evaluated using potentio-dynamic polarization and electrochemical impedance spectroscopy (EFM) at both pH 4 and pH 7, with a temperature of 30 °C, as presented in Table 1. The corrosion potential (E_{corr}), corrosion current density (I_{corr}), Tafel slopes (β_a and β_c), and corrosion rate (k) were determined for each alloy under both acidic and neutral conditions. The analysis of these electrochemical parameters provides valuable insights into the corrosion resistance and stability of these nanocomposite materials in different environments.

3.4.1. Electrochemical kinetic parameters. In Table 1a, the corrosion current density (I_{corr}) and corrosion potential (E_{corr}) values for the alloys at pH 4 and pH 7 suggest differing levels of corrosion resistance depending on the additive used. The results indicate that the Ti alloy exhibited the highest corrosion current density (I_{corr} = 43.08 μA cm^{-2} at pH 4), which suggests that it is more susceptible to corrosion compared to the Al, Cu, and W alloys. This could be due to the inherent properties of titanium, which, while highly resistant to corrosion in certain environments, may be less stable in acidic conditions. In contrast, the alloys with copper (Cu) and aluminum (Al) additives exhibited lower corrosion current densities, which suggests that these alloys are more resistant to corrosion under acidic conditions. At pH 7, the corrosion current densities were generally lower for all alloys, indicating improved corrosion resistance in neutral environments. The W and Ti alloys still showed relatively high I_{corr} values (33.77 μA cm^{-2} and 46.15 μA cm^{-2}, respectively), while Cu and Al alloys exhibited significantly lower values, reflecting better corrosion resistance in neutral conditions. These results suggest that the inclusion of Cu and Al additives may improve the overall stability of the alloys in physiological environments, which is critical for biomedical applications such as implants.

3.4.2. Corrosion potentials. In Table 1b, the corrosion potentials (E_{corr}) for the alloys in the two different pH environments also revealed important trends. At pH 4, the corrosion potentials for Ti and W alloys were more negative (−310 mV and −391 mV, respectively), indicating a higher tendency to corrode in acidic conditions. On the other hand, Al and Cu

Table 1 (a) Electrochemical kinetic parameters obtained *via* the EFM technique for various alloys at pH = 4 and pH = 7 at 30 °C, (b) electrochemical parameters for various alloys at pH = 4 and pH = 7 obtained *via* polarization measurements at 30 °C, (c) electrochemical corrosion coefficient values for titanium alloys grown in two different biological solutions at 37 °C *via* Tafel diagram analyses, and (d) the values of E_{pit} and E_{prot} for the Ti implant alloy in two biological solutions at 37 °C with a scan rate of 10 mV s^{-1}

pH	Alloy	I_{corr} (μA cm^{-2})	β_a (mV dec^{-1})	β_c (mV dec^{-1})	CF-2	CF-3	k (mpy)
(a)							
4	Al	1.128	117.6	122.4	1.459	3.407	0.5156
	Cu	1.248	52.1	62.98	1.239	2.762	0.5704
	Ti	43.08	228.8	256.9	2.094	1.206	19.69
	W	30.89	131.3	135.4	2.827	5.797	14.11
7	Al	1.471	86.3	87.88	1.316	9.534	0.6723
	Cu	1.612	169.9	183	1.108	826.4	0.7367
	Ti	46.15	221.8	248.2	2.065	842.1	21.09
	W	33.77	148.9	155.7	1.755	9.743	15.43

pH	Alloy	E_{corr} *vs.* SCE (mV)	I_{corr} (μA cm^{-2})	β_a (mV dec^{-1})	β_c (mV dec^{-1})	k (mpy)
(b)						
4	Al	−85.8	14.4	1679	1663	6.588
	Cu	−104	7.88	609.2	636.6	3.602
	Ti	−310	39.7	588.5	471.4	18.16
	W	−391	154	2214	865.6	70.37
7	Al	−109	11.9	813.7	797.8	5.432
	Cu	−53.7	1.41	337.6	320.6	0.6448
	Ti	−313	38.3	697.3	477.7	17.51
	W	−393	109	1702	831.9	50.02

	Parameters			
Solutions	β_a (mV decade^{-1})	$-\beta_c$ (mV decade^{-1})	I_{corr} (μA cm^{-2})	E_{corr} (V)
(c)				
Serum	85	50	0.35	−0.480
Urine	125	100	0.18	−0.430

	Parameters				
Solutions	$E_{corr,s}$ (V)	$E_{corr,f}$ (V)	E_{pit} (V)	E_{prot} (V)	I_{corr} (μA cm^{-2})
(d)					
Serum	−0.460	−0.312	−0.180	−0.150	11.4
Urine	−0.430	−0.115	0.2	−0.040	4.1

Open Access Article. Published on 12 December 2024. Downloaded on 4/2/2026 4:53:51 PM. This article is licensed under a Creative Commons Attribution 3.0 Unported Licence.

alloys exhibited less negative E_{corr} values (−85.8 mV and −104 mV), suggesting that these materials may provide better protection against corrosion in acidic conditions.

At pH 7, the corrosion potential is less negative for all alloys, with E_{corr} values for Cu and Al alloys being significantly more positive compared to Ti and W alloys. This reinforces the conclusion that Cu and Al additions enhance the corrosion resistance of the alloys in neutral conditions. These findings highlight the importance of adjusting alloy composition to optimize performance in specific environmental conditions.

3.4.3. Corrosion rates (k) and protection. In Table 1(a, b): the corrosion rates (k) in mpy (mils per year) further support the trends observed in the corrosion potential and current density data. Alloys with lower I_{corr} values, such as the Cu and Al doped alloys, exhibit reduced corrosion rates, indicating that these materials are better suited for applications, where longevity and stability are critical, such as in implants or protective coatings. The higher corrosion rates for the Ti and W alloys may limit their applicability in such environments unless further alloy modifications are made.

In Table 1c the cyclic voltammograms of Ti and the alloy were analyzed in serum and urine at 37 °C to investigate their corrosion behavior. In serum, the anodic Tafel slope (β_a) was 85 mV decade^{-1}, the cathodic Tafel slope ($-\beta_c$) was 50 mV decade^{-1}, the corrosion current density (I_{corr}) was 0.35 μA cm^{-2}, and the corrosion potential (E_{corr}) was −0.480 V. In urine, β_a increased to 125 mV decade^{-1}, $-\beta_c$ doubled to 100 mV decade^{-1}, I_{corr} decreased significantly to 0.18 μA cm^{-2}, and E_{corr} shifted to −0.430 V. These findings suggest a lower corrosion rate in urine compared to serum, highlighting the influence of electrolyte composition on the electrochemical performance of these alloys.

The electrochemical performance of the Ti implant alloy in serum and urine at 37 °C, evaluated using a scan rate of 10 mV s^{-1} as evaluated in Table 1d. The findings show distinct behaviors. In serum, the corrosion potentials ($E_{corr,s}$ and $E_{corr,f}$)

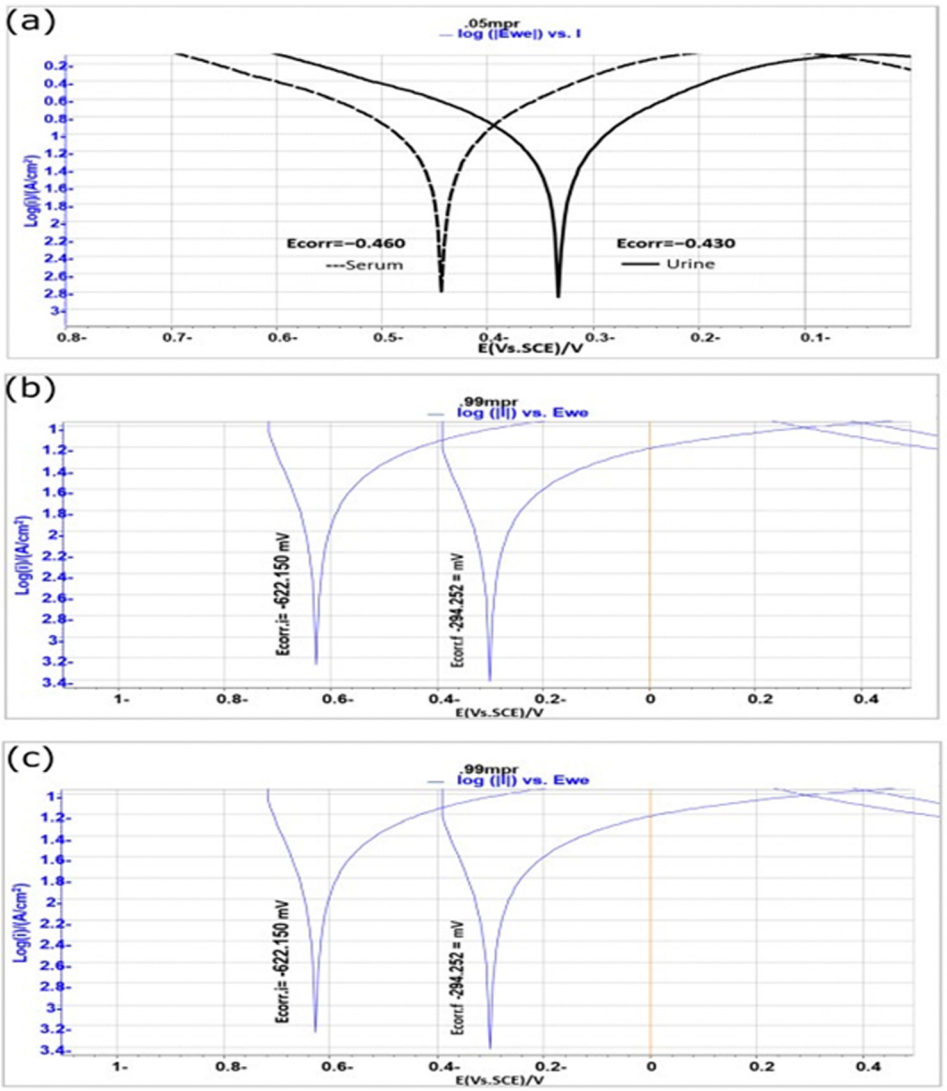

Fig. 3 (a) Cyclic voltammograms for the Ti implant, (b) for the Al implant, and (c) for the W implant in two biological solutions at a scan rate of 10 mV s^{-1}: urine and serum at 37 °C.

 © 2025 The Author(s). Published by the Royal Society of Chemistry

Open Access Article. Published on 12 December 2024. Downloaded on 4/2/2026 4:53:51 PM. This article is licensed under a Creative Commons Attribution 3.0 Unported Licence.

were −0.460 V and −0.312 V, with a pitting potential (E_{pit}) of −0.180 V, a protection potential (E_{prot}) of −0.150 V, and a corrosion current density (I_{corr}) of 11.4 μA cm^{-2}. In urine, $E_{corr,s}$ and $E_{corr,f}$ shifted positively to −0.430 V and −0.115 V, respectively, while E_{pit} increased significantly to 0.2 V, E_{prot} improved to −0.040 V, and I_{corr} dropped markedly to 4.1 μA cm^{-2}. These results indicate that while the Ti alloy exhibits superior resistance to pitting corrosion in urine, reflected by the higher E_{pit} and E_{prot} values, the significantly lower I_{corr} suggests better overall corrosion resistance in urine compared to serum. This behavior highlights the influence of electrolyte composition on the alloy's stability and performance.

3.4.4. Polarization measurements and biological solutions. Fig. 3 shows the cyclic voltammograms for Ti, Al, and W alloys in two biological electrolyte solutions, serum and urine, at 37 °C. The Tafel plots indicate that Ti implants exhibit superior corrosion resistance in serum compared to urine, with a wider passive region and lower corrosion current density (I_{corr}). This behavior is attributed to the formation of a stable oxide layer on the titanium surface, which protects the material from further corrosion in serum. However, the I_{corr} values in urine are higher, suggesting that the oxide layer is less stable or less protective in this medium. For Al alloys, the polarization data suggest moderate corrosion resistance in both serum and urine, with corrosion current densities ranging between 0.25–0.34 μA cm^{-2}. This indicates that Al implants may offer an intermediate level of corrosion resistance in biological environments, making them suitable for certain applications but less durable than Ti in the long term.

W alloys displayed higher corrosion current densities in both biological solutions, with values ranging from 0.25 μA cm^{-2} in serum to 0.34 μA cm^{-2} in urine. The results suggest that while W may provide adequate corrosion resistance, its performance in biological environments may be surpassed by that of Ti and Al alloys, particularly for applications requiring long-term durability. These electrochemical corrosion tests provide a clear comparison of the corrosion behavior of the various alloys in different pH environments and biological solutions. The data strongly indicate that Cu and Al alloys exhibit superior corrosion resistance, particularly in neutral and acidic conditions, making them promising candidates for applications in harsh environments. The results also emphasize the need to tailor alloy composition and processing conditions to achieve the desired balance of mechanical and corrosion properties for specific applications, such as in biomedical implants or protective coatings.

$E_{corr,f}$ is the final corrosion, and $E_{corr,s}$ is the starting corrosion potential after reversing the scan direction. E_{pit}, also known as the pitting potential, is characterized by a continuous increase in the anodic current. Similarly, the protection potential (E_{prot}) refers to the potential where the reverse scan intersects the forward scan, completing the hysteresis loop. (β_a and $-\beta_c$), and corrosion potentials were obtained from Tafel analyses based on cyclic voltammetry (CV) curves. Log(i)/(A cm^{-2}).

The experimental data of the corrosion potentials are tabulated in Table 2. Table 2(a) shows the cyclic voltammograms recorded for composites doped with Al and the alloy in

Table 2 (a) Electrochemical corrosion coefficient values for Al alloys grown in three different biological solutions at 37 °C *via* Tafel diagram analysis. (b) Values of E_{pit} and E_{prot} for the Cu implant alloy in two biological solutions at 37 °C with a scan rate of 10 mV s^{-1}. (c) Electrochemical corrosion coefficient values for the W implant alloy grown in three different biological solutions at 37 °C *via* Tafel diagram analysis. (d) The values of E_{pit} and E_{prot} for the Ti implant alloy in two biological solutions at 37 °C with a scan rate of 10 mV s^{-1} (β_a and $-\beta_c$) and corrosion potentials were obtained from Tafel analyses *via* cyclic voltammetry (CV) curves

	Parameters			
Solutions	β_a (mV decade^{-1})	$-\beta_c$ (mV decade^{-1})	I_{corr} (μA cm^{-2})	E_{corr} (V)
(a)				
Serum	80	190	0.34	−0.120
Urine	143	129	0.25	−0.194

	Parameters				
Solutions	$E_{corr,s}$ (V)	$E_{corr,f}$ (V)	E_{pit} (V)	E_{prot} (V)	I_{corr} (μA cm^{-2})
(b)					
Serum	−0.812	−0.815	−0.80	−0.250	7.4
Urine	−0.294	−0.298	−0.285	−0.155	5.12

	Parameters			
Solutions	β_a (mV decade^{-1})	$-\beta_c$ (mV decade^{-1})	I_{corr} (μA cm^{-2})	E_{corr} (V)
(c)				
Serum	92	43	0.214	−0.321
Urine	107	92	0.318	−0.374

	Parameters				
Solutions	$E_{corr,s}$ (V)	$E_{corr,f}$ (V)	E_{pit} (V)	E_{prot} (V)	I_{corr} (μA cm^{-2})
(d)					
Serum	−0.380	−0.271	−0.261	−0.122	12.48
Urine	−0.358	−0.207	0.300	−0.086	22.21

biological electrolyte solutions (serum and urine) at 37 °C to evaluate their corrosion behavior. In serum, the anodic Tafel slope (β_a) was 80 mV decade^{-1}, the cathodic Tafel slope ($-\beta_c$) was 190 mV decade^{-1}, the corrosion current density (I_{corr}) was 0.34 μA cm^{-2}, and the corrosion potential (E_{corr}) was −0.120 V. In urine, β_a increased to 143 mV decade^{-1}, $-\beta_c$ decreased to 129 mV decade^{-1}, I_{corr} decreased to 0.25 μA cm^{-2}, and E_{corr} shifted to −0.194 V. These results indicate that the alloys exhibit distinct electrochemical behaviors in the two electrolytes, reflecting differences in corrosion kinetics and passivation.

The results of the electrochemical behavior of a Cu implant alloy were evaluated in serum and urine at 37 °C using a scan rate of 10 mV s^{-1} presented in Table 2(b). In serum, the start and final corrosion potentials ($E_{corr,s}$ and $E_{corr,f}$) were −0.812 V and −0.815 V, respectively, while the pitting potential (E_{pit}) was −0.80 V, the protection potential (E_{prot}) was −0.250 V, and the corrosion current density (I_{corr}) was 7.4 μA cm^{-2}. In urine, $E_{corr,s}$ and $E_{corr,f}$ shifted to −0.294 V and −0.298 V, respectively, with E_{pit} at −0.285 V, E_{prot} at −0.155 V, and I_{corr} reduced to 5.12 μA cm^{-2}. These results indicate enhanced corrosion resistance of the Cu alloy in urine compared to serum, as evidenced by the higher E_{prot} and lower I_{corr} values.

The electrochemical corrosion behavior of a W implant alloy was investigated in serum and urine at 37 °C using the Tafel

Open Access Article. Published on 12 December 2024. Downloaded on 4/2/2026 4:53:51 PM.
This article is licensed under a Creative Commons Attribution 3.0 Unported Licence.

diagram analysis depicted in Table 2(c). In serum, the anodic Tafel slope (β_a) was 92 mV decade^{-1}, the cathodic Tafel slope ($-\beta_c$) was 43 mV decade^{-1}, the corrosion current density (I_{corr}) was 0.214 μA cm^{-2}, and the corrosion potential (E_{corr}) was −0.321 V. In urine, β_a increased to 107 mV decade^{-1}, $-\beta_c$ more than doubled to 92 mV decade^{-1}, I_{corr} rose to 0.318 μA cm^{-2}, and E_{corr} shifted to −0.374 V. These findings suggest a higher corrosion rate in urine compared to serum, indicated by the increased I_{corr} and more negative E_{corr} values, reflecting the electrolyte's impact on the corrosion kinetics of the W alloy.

The electrochemical behavior of a Ti implant alloy in serum and urine at 37 °C was analyzed using Tafel analyses *via* cyclic voltammetry (CV) curves, as shown in Table 2(d), with a scan rate of 10 mV s^{-1}. Key parameters, including corrosion and protection potentials as well as current densities, were measured to assess corrosion resistance. In serum, the initial and final corrosion potentials ($E_{corr,s}$ and $E_{corr,f}$) were −0.380 V and −0.271 V, respectively, with a pitting potential (E_{pit}) of −0.261 V, a protection potential (E_{prot}) of −0.122 V, and a corrosion current density (I_{corr}) of 12.48 μA cm^{-2}. Comparatively, in urine, $E_{corr,s}$ and $E_{corr,f}$ shifted to −0.358 V and −0.207 V, respectively, while E_{pit} increased significantly to 0.300 V, E_{prot} rose to −0.086 V, and I_{corr} was markedly higher at 22.21 μA cm^{-2}. The data indicate that while the Ti alloy exhibited a higher resistance to pitting corrosion in urine, as evidenced by the elevated E_{pit}, the increased I_{corr} suggests a greater general corrosion rate in urine compared to serum. This highlights the influence of electrolyte composition on the alloy's electrochemical stability and overall corrosion behavior.

The comparison of the data of the electrochemical behavior of Al, Cu, W, and Ti implant alloys in biological solutions at 37 °C reveals distinct corrosion characteristics that can be concluded as: Al alloy exhibits moderate corrosion resistance, with intermediate I_{corr} and E_{corr} values influenced by the electrolyte. But the Cu alloy shows higher corrosion rates in serum (I_{corr} = 7.4 μA cm^{-2}) compared to urine (I_{corr} = 5.12 μA cm^{-2}) but demonstrates better pitting resistance in urine. Meanwhile, the W alloy displays a relatively low I_{corr} in serum (0.214 μA cm^{-2}), indicating good corrosion resistance, though urine increases its corrosion rate. Finally, the Ti alloy, while it has better pitting resistance in urine (E_{pit} = 0.300 V), its higher I_{corr} in urine (22.21 μA cm^{-2}) suggests increased general corrosion compared to serum. Overall, Ti and Cu alloys show significant sensitivity to electrolyte composition, while W generally offers higher stability.

3.5. Biological and immunogenic effects of the intraperitoneal injection of different alloys

The biological and immunogenic responses of male albino rats following the intraperitoneal (i.p.) injection of various alloy materials at different doses over a subacute duration of 60 days were then explored. The alloys tested include aluminum (Al),

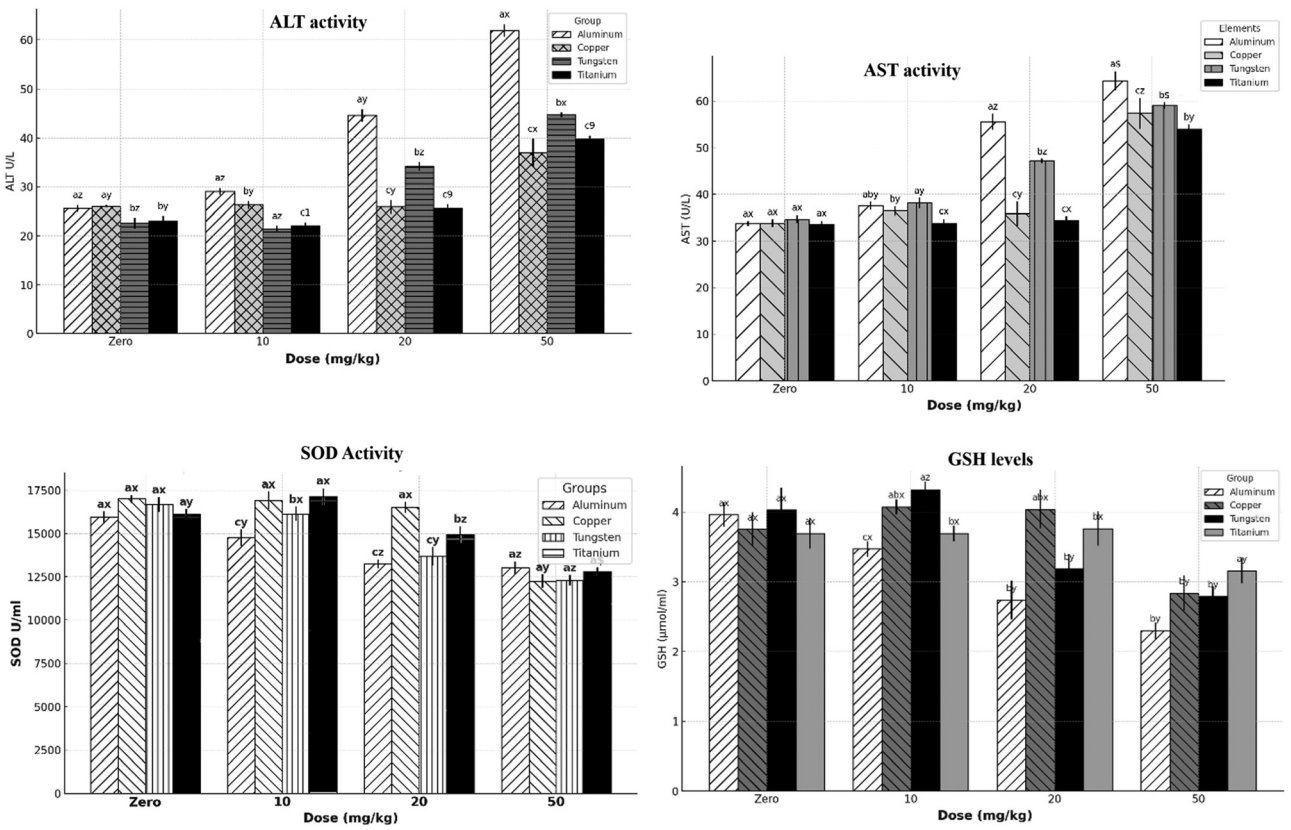

Fig. 4 Multivariate analysis of the effects of different alloyed materials on liver function marker enzyme in rats scattered in a dose-dependent manner on serum levels of ALT, serum levels of AST, and oxidative stress markers, SODs, and hepatic level of GSH, in rats scattered in a dose-dependent manner.

© 2025 The Author(s). Published by the Royal Society of Chemistry

Open Access Article. Published on 12 December 2024. Downloaded on 4/2/2026 4:53:51 PM.
This article is licensed under a Creative Commons Attribution 3.0 Unported Licence.

copper (Cu), tungsten (W), and titanium (Ti), which were administered at three dose levels: 10 mg kg^{-1}, 20 mg kg^{-1}, and 50 mg kg^{-1} body weight (BW). Liver function, oxidative stress markers, and immunological responses were monitored throughout the study, with the data presented in Fig. 4.

3.5.1. Liver function (ALT and AST). The assessment of liver enzymes (ALT and AST) revealed significant dose-dependent changes in all treated groups, reflecting the systemic impact of the alloys. Fig. 4(a) illustrates the serum ALT activities for the different alloys at various doses. Notably, aluminum and titanium exhibited marked increases in ALT levels at the medium (20 mg kg^{-1}) and high (50 mg kg^{-1}) doses, with aluminum showing particularly elevated levels. This indicates hepatocellular damage, as ALT leakage into the bloodstream is a known marker of liver injury. In contrast, copper demonstrated the least impact on ALT levels, maintaining enzyme activity within normal ranges even at higher doses, particularly at the 20 mg kg^{-1} and 50 mg kg^{-1} BW doses. Tungsten and titanium, while showing less dramatic increases than aluminum, still demonstrated some liver toxicity at higher doses. These findings suggest that copper may have superior biocompatibility in terms of hepatic function, compared to the other metals in this study.

The AST levels in Fig. 4(b) support these observations, showing a similar pattern. Significant increases in AST were noted in the aluminum and tungsten groups, especially at higher doses, while copper and titanium exhibited more moderate increases in AST activity. These results align with the observed changes in ALT, suggesting a dose-dependent liver damage associated with the alloys, particularly aluminum and tungsten.

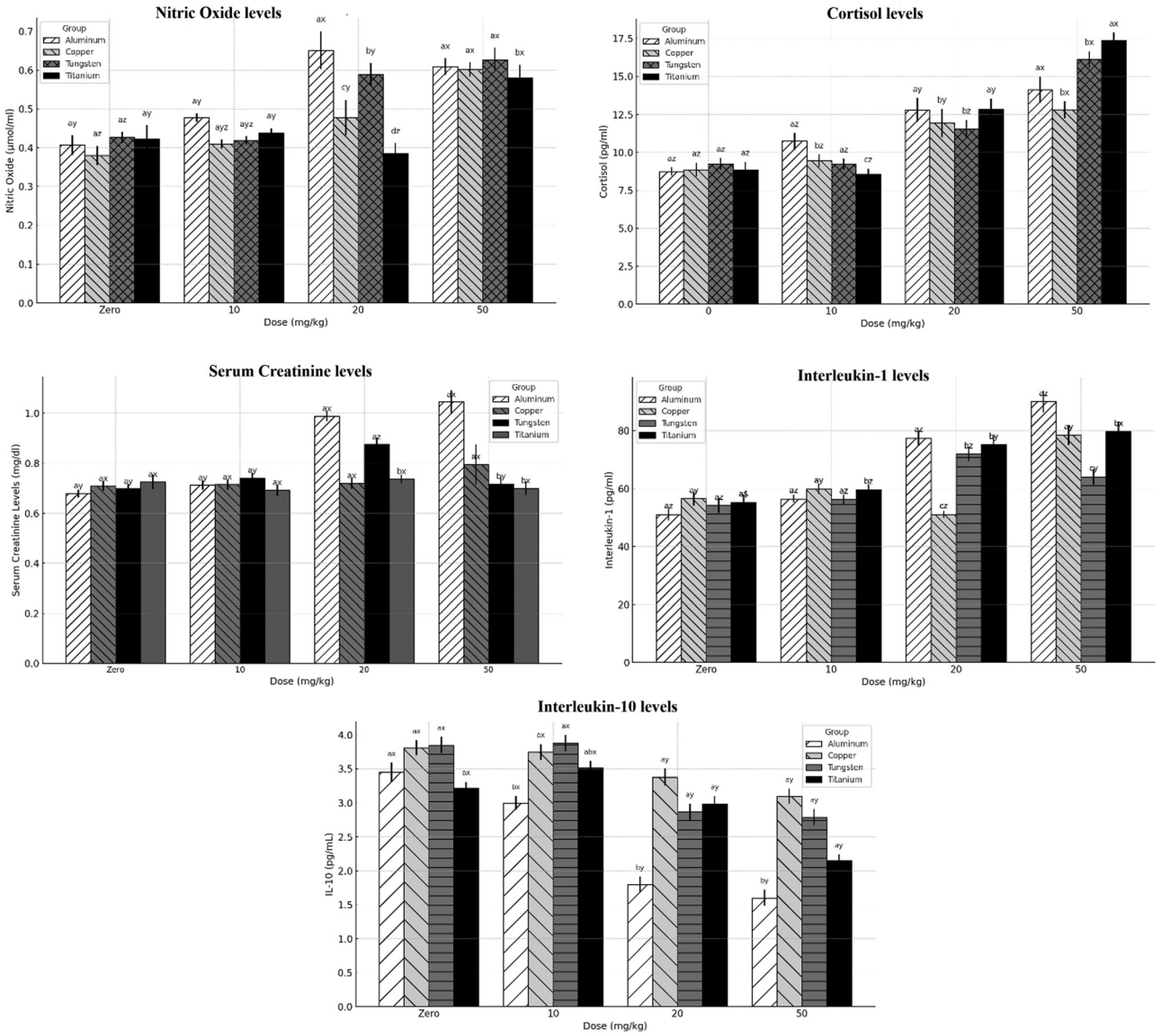

Fig. 5 Multivariate analysis of the effects of different alloy materials on the following: nitrosative stress markers (nitric oxide), serum cortisol level (as a stress marker) in rats scattered in a dose-dependent manner, serum creatinine level (as a renal performance marker), serum IL-1 level (as an immune response marker) and serum IL-10 level in rats scattered in a dose-dependent manner.

Open Access Article. Published on 12 December 2024. Downloaded on 4/2/2026 4:53:51 PM.
This article is licensed under a Creative Commons Attribution 3.0 Unported Licence.

3.5.2. Oxidative stress and antioxidant enzyme activity (SOD and GSH). The assessment of oxidative stress markers, including SOD and GSH, revealed important insights into the alloys' effects on the rat's antioxidant defense system. Fig. 4(c) shows significant reductions in SOD activity in rats treated with aluminum and tungsten, particularly at the 50 mg kg^{-1} BW dose. This suggests that these alloys induce oxidative stress, depleting antioxidant defenses. Interestingly, copper exhibited relatively stable SOD activity, particularly at lower doses, suggesting that copper may mitigate oxidative damage more effectively than the other alloys. The GSH levels presented in Fig. 4(d) also reflected the effects of oxidative stress. GSH levels were significantly lower in the aluminum and tungsten groups at the medium and high doses, further indicating that these alloys provoke oxidative damage. On the other hand, copper and titanium groups exhibited less reduction in GSH levels, with copper maintaining higher GSH concentrations across all doses. This supports the hypothesis that copper may have a protective effect against oxidative damage, potentially explaining its more favorable liver function results.

3.5.3. Nitric oxide (NO) and immune response (cortisol, IL-1, and IL-10). In terms of nitrosative stress, the data from Fig. 5(a) demonstrate that all alloys except titanium induced increased levels of nitric oxide (NO) at the 50 mg kg^{-1} dose. This surge in NO production suggests the onset of inflammatory responses and liver damage. The titanium group showed a more favorable profile with minimal alterations in NO levels, which is consistent with its more moderate impact on liver function and oxidative stress. The cortisol levels, measured as an indicator of stress, were significantly elevated in all treatment groups at the higher doses (50 mg kg^{-1}), with the aluminum group showing the most pronounced increase in serum cortisol Fig. 5(b). Copper, however, appeared to be the least disruptive to the stress response, with less of an increase in cortisol levels, supporting its role in mitigating stress-induced effects. The tungsten and titanium groups showed moderate increases in cortisol, indicating a dose-dependent stress response, though these increases were less pronounced than those observed for aluminum. In terms of immune response, interleukin-1 (IL-1) concentrations in Fig. 5(d) were elevated in the aluminum and tungsten groups at the higher doses, reflecting an inflammatory immune response. Conversely, copper exhibited a more stable IL-1 profile, with significantly lower levels of IL-1 at the 20 mg kg^{-1} and 50 mg kg^{-1} doses, suggesting a more favorable immune response. Titanium showed intermediate IL-1 levels, which were significantly lower than those of aluminum and tungsten, aligning with its relatively mild biological effects. IL-10, an anti-inflammatory cytokine, was notably elevated in the copper group, indicating a potential modulatory effect on immune response Fig. 5(e). This anti-inflammatory response was not observed in the aluminum and tungsten groups, where IL-10 levels decreased at higher doses, suggesting that these alloys provoke a more pronounced inflammatory response.

3.5.4. Nephrotoxicity (creatinine). Lastly, serum creatinine levels, which are indicative of renal function, were significantly altered in the treated groups, particularly at the 50 mg kg^{-1} dose (Fig. 5(c)). While copper did not significantly affect creatinine levels across any dose, aluminum and tungsten exhibited substantial increases in serum creatinine at higher doses, suggesting nephrotoxic effects. Titanium also showed minimal changes in creatinine levels, reinforcing its more favorable biocompatibility profile compared to the other alloys.

4. Conclusions

Nickel-free porous stainless steels composed of F2581 (Fe–17Cr–10Mn–3MX–0.4Si–0.5 N–0.2C in wt%; MX = Al, Cu, Ti, and W) were synthesized *via* a solid-state reaction method. The XRD pattern revealed the crystal structure of the Fe phase. The crystallite sizes are approximately 73, 27.2, 76, and 98.5 nm for samples with Al, Cu, Ti, and W, respectively. The morphology of the synthesized nanoparticles is as follows: nanowires, square nanotubes, wave-like (growing clover farm) and nanofibers for Al, Cu, Ti, and W ions with nanopores distributed in shapes, respectively. The experimental data revealed that the samples with Cu and Ti seemed to be the most suitable for medical implantation and biological macromolecule applications. Furthermore, the electrochemical kinetic parameters were obtained *via* two different methods: EFM and polarized techniques. In our practical study of electrochemical corrosion properties of three alloys (Ti, Al, and W) grown in biological solutions by electrochemical techniques, the results revealed that, compared with those of other alloys in serum and urine, the corrosion resistance of Ti alloy in blood serum was the highest. A pilot study evaluating the biological performance and immunogenicity of these alloys revealed that the high dose of each alloy induced biological alterations and introduced immunogenicity at high doses. In contrast, Cu, W, and Ti at low doses are safer and do not present any immune response for subacute doses, and the medium dose exhibited the same response but for Cu only.

Author contributions

S. A. Abdelwahab, M. Zewaid and A. I. Ali: fabricated and characterized the samples. Mohamad Warda, Omar A. Ahmed-Farid and Hassan A. M. Hendawy: investigated the results of electrochemical and biological experiments. H. Saleh, J. Y. Son, M. Warda, O. A. Ahmed-Farid, H. A. M. Hendawy, A. I. Ali, A. Negm and E. A. Kamoun: contributed to the analysis of the data and writing and reviewed the final manuscript. All authors approve the final version of the submission.

Ethical approval

The experimental procedures adhered strictly to the ethical guidelines established by the Institutional Animal Care and Use Committee (IACUC) at the Faculty of Veterinary Medicine, Cairo University, Egypt (Approval No: Vet CU. 09092023786), as well as the ethical standards outlined by the National Organization

© 2025 The Author(s). Published by the Royal Society of Chemistry

Open Access Article. Published on 12 December 2024. Downloaded on 4/2/2026 4:53:51 PM. This article is licensed under a Creative Commons Attribution 3.0 Unported Licence.

for Drug Control and Research. All procedures were performed in accordance with the NC3Rs ARRIVE Guidelines. For the human blood and urine donated samples, the signed consents of the donors (of 5 persons) were first taken before the experiment start according to the research ethical rules in Egyptian Universities.

Data availability

The datasets used and/or analyzed during the current study are available from the corresponding author upon reasonable request. In addition, all the data generated or analyzed during this study are included in this article.

Conflicts of interest

There are no conflicts of interest.

References

1 S. Wu, *et al.*, Biomimetic porous scaffolds for bone tissue engineering, *Mater. Sci. Eng., R*, 2014, **80**, 1–36.
2 K.-H. Frosch and K. M. Stürmer, Metallic biomaterials in skeletal repair, *Eur. J. Trauma*, 2006, **32**, 149–159.
3 S. J. Hollister, Porous scaffold design for tissue engineering, *Nat. Mater.*, 2005, **4**(7), 518–524.
4 J. Čapek and D. Vojtěch, Effect of sintering conditions on the microstructural and mechanical characteristics of porous magnesium materials prepared by powder metallurgy, *Mater. Sci. Eng., C*, 2014, **35**, 21–28.
5 J. Čapek and D. Vojtěch, Microstructural and mechanical characteristics of porous iron prepared by powder metallurgy, *Mater. Sci. Eng., C*, 2014, **43**, 494–501.
6 J. Čapek, D. Vojtěch and A. Oborná, Microstructural and mechanical properties of biodegradable iron foam prepared by powder metallurgy, *Mater. Des.*, 2015, **83**, 468–482.
7 K. Alvarez and H. Nakajima, Metallic scaffolds for bone regeneration, *Materials*, 2009, **2**(3), 790–832.
8 V. Karageorgiou and D. Kaplan, Porosity of 3D biomaterial scaffolds and osteogenesis, *Biomaterials*, 2005, **26**(27), 5474–5491.
9 S. Jayasathyakawin, *et al.*, A Review on Exploration of Magnesium Matrix Composites, *Mater. Sci. Forum*, 2022, **1068**, 63–70.
10 J. Jowsey, Studies of Haversian systems in man and some animals, *J. Anat.*, 1966, **100**(Pt 4), 857.
11 V. S. de Viteri and E. Fuentes, Titanium and titanium alloys as biomaterials, *Tribol.: Fundam. Adv.*, 2013, **1**(5), 154–181.
12 M. Saini, *et al.*, Implant biomaterials: a comprehensive review, *World J. Clin. Cases*, 2015, **3**(1), 52.
13 H. Shi, *et al.*, Functional gradient metallic biomaterials: techniques, current scenery, and future prospects in the biomedical field, *Front. Bioeng. Biotechnol.*, 2021, **8**, 616845.
14 X. Zhang, *et al.*, Preparation and mechanical property of a novel 3D porous magnesium scaffold for bone tissue engineering, *Mater. Sci. Eng., C*, 2014, **42**, 362–367.
15 B. Arifvianto and J. Zhou, Fabrication of metallic biomedical scaffolds with the space holder method: a review, *Materials*, 2014, **7**(5), 3588–3622.
16 S. Bose, S. Vahabzadeh and A. Bandyopadhyay, Bone tissue engineering using 3D printing, *Mater. today*, 2013, **16**(12), 496–504.
17 X. Wang, *et al.*, Porous TiNbZr alloy scaffolds for biomedical applications, *Acta Biomater.*, 2009, **5**(9), 3616–3624.
18 E. Babaie and S. B. Bhaduri, Fabrication aspects of porous biomaterials in orthopedic applications: a review, *ACS Biomater. Sci. Eng.*, 2018, **4**(1), 1–39.
19 J. Parthasarathy, B. Starly and S. Raman, A design for the additive manufacture of functionally graded porous structures with tailored mechanical properties for biomedical applications, *J. Manuf. Process.*, 2011, **13**(2), 160–170.
20 V. Geantă, *et al.*, Stainless steels with biocompatible properties for medical devices, *Key Eng. Mater.*, 2014, **583**, 9–15.
21 K. Essa, *et al.*, Porosity control in 316 L stainless steel using cold and hot isostatic pressing, *Mater. Des.*, 2018, **138**, 21–29.
22 M. Resnik, *et al.*, Strategies for improving antimicrobial properties of stainless steel, *Materials*, 2020, **13**(13), 2944.
23 Q. Chen and G. A. Thouas, Metallic implant biomaterials, *Mater. Sci. Eng., R*, 2015, **87**, 1–57.
24 E. Davoodi, *et al.*, Additively manufactured metallic biomaterials, *Bioact. Mater.*, 2022, **15**, 214–249.
25 T. Murakami, T. Akagi and E. Kasai, Development of porous iron based material by slag foaming and its reduction, *Proc. Mater. Sci.*, 2014, **4**, 27–32.
26 J. Čapek, *et al.*, Highly porous, low elastic modulus 316 L stainless steel scaffold prepared by selective laser melting, *Mater. Sci. Eng., C*, 2016, **69**, 631–639.
27 Z. Li, *et al.*, A sol–gel-derived α-Al_2O_3 crystal interlayer modified 316 L porous stainless steel to support TiO_2, SiO_2, and TiO_2–SiO_2 hybrid membranes, *J. Mater. Sci.*, 2011, **46**, 3127–3135.
28 S. D. F. F. Mariotto, *et al.*, Porous stainless steel for biomedical applications., *Mater. Res.*, 2011, **14**, 146–154.
29 F. M. Noor, K. Jamaludin and S. Ahmad, Fabrication of porous stainless steel 316 L for biomedical applications, *MATEC Web Conf.*, 2017, **135**, 7.
30 M. M. Dewidar, K. A. Khalil and J. Lim, Processing and mechanical properties of porous 316 L stainless steel for biomedical applications, *Trans. Nonferrous Met. Soc. China*, 2007, **17**(3), 468–473.
31 E. Salahinejad, *et al.*, Microstructure and wear behavior of a porous nanocrystalline nickel-free austenitic stainless steel developed by powder metallurgy, *Mater. Des.*, 2010, **31**(4), 2259–2263.
32 A. Dudek and R. Włodarczyk, Effect of sintering atmosphere on properties of porous stainless steel for biomedical applications, *Mater. Sci. Eng., C*, 2013, **33**(1), 434–439.
33 M. Zielecka, *et al.*, Silicone resin-based intumescent paints, *Materials*, 2020, **13**(21), 4785.

Open Access Article. Published on 12 December 2024. Downloaded on 4/2/2026 4:53:51 PM. This article is licensed under a Creative Commons Attribution 3.0 Unported Licence.

34 T. K. Tatt, *et al.*, Production of porous stainless steel using the space holder method, *Sains Malays.*, 2021, **50**, 507–514.
35 W. Zhang, *et al.*, The Effect of Porosity on Mechanical Properties of Porous FeCrN Stainless Steel, *J. Phys.: Conf. Ser.*, 2021, **2044**, 012002.
36 B. Vandenbroucke and J. P. Kruth, Selective laser melting of biocompatible metals for rapid manufacturing of medical parts, *Rapid Prototyping J.*, 2007, **13**(4), 196–203.
37 D. K. Pattanayak, *et al.*, Bioactive Ti metal analogous to human cancellous bone: fabrication by selective laser melting and chemical treatments, *Acta Biomater.*, 2011, **7**(3), 1398–1406.
38 M. Ramirez-del-Solar and E. Blanco, Porous thin films from sol–gel, *Submicron porous materials*, 2017, 157–188.
39 S. A. Yavari, *et al.*, Fatigue behavior of porous biomaterials manufactured using selective laser melting, *Mater. Sci. Eng., C*, 2013, **33**(8), 4849–4858.
40 A. S. Idil and N. Donaldson, The use of tungsten as a chronically implanted material, *J. Neural Eng.*, 2018, **15**(2), 021006.
41 M. Rahmati and M. Mozafari, Biocompatibility of alumina-based biomaterials–A review, *J. Cell. Physiol.*, 2019, **234**(4), 3321–3335.
42 Q. Shen, *et al.*, Advances in copper-based biomaterials with antibacterial and osteogenic properties for bone tissue engineering, *Front. Bioeng. Biotechnol.*, 2022, **9**, 795425.
43 M. Javanbakht, M. Hadianfard and E. Salahinejad, Microstructure and mechanical properties of a new group of nanocrystalline medical-grade stainless steels prepared by powder metallurgy, *J. Alloys Compd.*, 2015, **624**, 17–21.
44 G. A. Perchetti, *et al.*, Stability of SARS-CoV-2 in phosphate-buffered saline for molecular detection, *J. Clin. Microbiol.*, 2020, **58**(8), 1–3.
45 H. Savaloni, *et al.*, Influence of N+ implantation on structure, morphology, and corrosion behavior of Al in NaCl solution, *Chin. Phys. B*, 2020, **29**(5), 058102.
46 D. M. Cocchetto and T. D. Bjornsson, Methods for vascular access and collection of body fluids from the laboratory rat, *J. Pharm. Sci.*, 1983, **72**(5), 465–492.
47 S. Reitman and S. Frankel, Calorimetric method for the determination of blood aminotransferase enzymatic activities, *Am. J. Clin. Pathol.*, 1957, **28**, 56–63.
48 S. Marklund and G. Marklund, Involvement of the superoxide anion radical in the autoxidation of pyrogallol and a convenient assay for superoxide dismutase, *Eur. J. Biochem.*, 1974, **47**(3), 469–474.
49 E. Jayatilleke and S. Shaw, A high-performance liquid chromatographic assay for reduced and oxidized glutathione in biological samples, *Anal. Biochem.*, 1993, **214**(2), 452–457.
50 I. Papadoyannis, V. Samanidou and C. C. Nitsos, Simultaneous determination of nitrite and nitrate in drinking water and human serum by high performance anion-exchange chromatography and UV detection, *J. Liq. Chromatogr. Relat. Technol.*, 1999, **22**(13), 2023–2041.
51 H. Yang, *et al.*, Facile preparation of super-hydrophobic and super-oleophilic silica film on stainless steel mesh via sol–gel process, *Appl. Surf. Sci.*, 2010, **256**(13), 4095–4102.
52 E. Salahinejad, R. Amini and M. Hadianfard, Effect of milling time on structure and mechanical properties of porous nickel-free austenitic stainless steels processed by mechanical alloying and sintering, *Mater. Sci. Eng., A*, 2010, **527**(21–22), 5522–5527.
53 Y. Zhou, Characterization of the porosity and pore behavior during the sintering process of 420 stainless steel samples produced with gas-and water-atomized powder using powder based 3-d printing, University of Pittsburgh, Swanson School of Engineering, 2014, pp. 1–88.
54 E. Salahinejad, *et al.*, Microstructural characterization of medical-grade stainless steel powders prepared by mechanical alloying and subsequent annealing, *Adv. Powder Technol.*, 2013, **24**(3), 605–608.
55 A. I. Ali and A. Hassen, Synthesis, characterization, ferroelectric, and piezoelectric properties of $(1-x)BaTiO_{3-x}$-$(BaNi_{0.5}Nb_{0.5}O_3)$ perovskite ceramics, *J. Mater. Sci.: Mater. Electron.*, 2021, **32**(8), 10769–10777.
56 A. I. Ali, *et al.*, Preparation, structural and dielectric properties of nanocomposite $Al_2O_3/BaTiO_3$ for multilayer ceramic capacitors applications, *J. Mater. Res. Technol.*, 2022, **18**, 2083–2092.
57 A. M. El Nahrawy, *et al.*, Talented $Bi_{0.5}Na_{0.25}K_{0.25}TiO_3$/oxidized cellulose films for optoelectronic and bioburden of pathogenic microbes, *Carbohydr. Polym.*, 2022, **291**, 119656.
58 A. M. El-Nahrawy, *et al.*, Influences of Ag-NPs doping chitosan/calcium silicate nanocomposites for optical and antibacterial activity, *Int. J. Biol. Macromol.*, 2016, **93**, 267–275.

© 2025 The Author(s). Published by the Royal Society of Chemistry